Journal of Translational Medicine

RESEARCH

Open Access

Histidine metabolism drives liver cancer progression via immune microenvironment modulation through metabolic reprogramming

Pengcheng Liu[1†], Fuxin Huang[3†], Peixu Lin[1], Jiayao Liu[3], Pincheng Zhou[3], Jie Wang[4], Huanhuan Sun[1*], Fan Xing[1*] and Haiqing Ma[2,1,3,4*]

Abstract

Background Histidine metabolism is crucial in role in tumor biology, contributing to tumor progression, immune regulation, and metabolic reprogramming. In hepatocellular carcinoma (HCC), dysregulated histidine metabolism may promote tumor growth and immune evasion, although the specific mechanisms remain poorly understood.

Methods Using single-cell RNA sequencing, the expression patterns of histidine metabolism–related genes were evaluated across different cell types in HCC samples. In vivo and in vitro experiments were conducted to validate how histidine treatment affects macrophage and T-cell function. Furthermore, the TCGA database was utilized to construct a prognostic model to identify the key gene BUD23 and to examine its correlation with metabolism and immune infiltration.

Results The proportion of parenchymal cells exhibiting high histidine metabolism was significantly increased, accompanied by a general reduction in immune and stromal cell infiltration. Notably, macrophages and T cells demonstrated impaired antitumor functions. In the high histidine metabolism group, multiple critical cell communication pathways (e.g., MIF, CLEC, MHC II) were downregulated, macrophages shifted toward immunosuppressive subpopulations, T cells exhibited an exhaustion phenotype, and CD8 + T-cell activation was diminished. Further in vivo and in vitro co-culture experiments confirmed that elevated histidine concentrations promoted M2 polarization in macrophages and weakened T-cell cytotoxicity, accelerating tumor proliferation. According to TCGA analyses, BUD23 was upregulated in the high histidine metabolism group and significantly negatively correlated with patient survival and immune cell infiltration. Silencing BUD23 boosted immune cell

†Pengcheng Liu and Fuxin Huang contributed equally to this work.

*Correspondence:
Huanhuan Sun
huanhuansun10@163.com
Fan Xing
xingfan@gdph.org.cn
Haiqing Ma
mahaiqing@gdph.org.cn

Full list of author information is available at the end of the article

activation and cytotoxic effects, effectively reversing the immunosuppressive microenvironment. A multivariable Cox regression–based prognostic model indicated unfavorable outcomes in patients with high histidine metabolism.

Conclusion Histidine metabolism drives tumor cell metabolic reprogramming and reshapes the tumor immune microenvironment through intercellular communication, thereby promoting tumor progression. BUD23 shows promise as a biomarker for prognosis and immune response prediction in liver cancer. This study provides new therapeutic targets and theoretical support for liver cancer treatment by targeting histidine metabolism.

Keywords Histidine metabolism, Hepatocellular carcinoma, Tumor microenvironment, Immune suppression, BUD23, Prognosis

Introduction

Histidine is an essential amino acid extensively involved in various physiological functions and metabolic pathways for the human body. Recent studies have shown that histidine metabolism is closely linked to the onset and progression of numerous diseases, particularly highlighting its role in cancer [1–3]. Liver cancer, specifically hepatocellular carcinoma (HCC), is among the most prevalent malignancies worldwide. Its pathogenesis is complex, involving dysregulation across multiple metabolic pathways [4–6], with changes in histidine metabolism potentially playing a significant role. Histidine metabolism primarily occurs through the decarboxylation catalyzed by histidine decarboxylase, producing histamine, which is subsequently metabolized into downstream products such as imidazole acetic acid. Additionally, histidine can undergo transamination to generate glutamate, which participates in energy metabolism, including the tricarboxylic acid (TCA) cycle [2, 7, 8]. Histidine metabolites, particularly histamine, play crucial roles not only in immune responses and inflammatory reactions [9–11] but also regulating the tumor microenvironment [12–14].

Metabolic reprogramming of hepatocytes is a key feature in the onset and progression of liver cancer [15–17]. Research has demonstrated that, to meet the demands of rapid proliferation, cancer cells alter their energy metabolism, including glycolysis, fatty acid metabolism, and amino acid metabolism [16, 18–21]. Histidine and its metabolites may contribute to liver cancer development through the following mechanisms: (1) Inflammation and Immune Regulation: Liver cancer onset is often accompanied by changes in the immune microenvironment, with histidine metabolites, such as histamine, playing pivotal roles in inflammatory responses. Histamine regulates immune cell functions, including T cells, B cells, macrophages, and dendritic cells-through its receptors (e.g., H1, H2, H3, and H4 receptors), thereby influencing the tumor immune microenvironment [9, 12–14]. Degradation products of histidine, such as urocanic acid, glutamate, and cis-urocanic acid, exhibit immunosuppressive properties, potentially promoting tumor development by inhibiting antitumor immune function [22]. (2) Oxidative Stress and Antioxidant Defense: Histidine metabolism is closely associated with the regulation of oxidative stress. Through its metabolites, histidine influences the redox state, contributing to the maintainance of intracellular antioxidant balance [23–28]. Liver cancer cells are frequently in a state of high oxidative stress, which promotes tumor cell survival and proliferation [29–32]. Targeting histidine metabolism or oxidative stress pathways may represent a potential therapeutic strategy for liver cancer. (3) Regulation of Energy Metabolism: Histidine metabolism is closely linked to the energy demands of liver cancer cells. Histidine contributes to the TCA cycle by generating glutamate, thereby impacting the energy supply of hepatocytes [2, 7]. In liver cancer, metabolic reprogramming drives increased energy requirements [15–17], and histidine metabolism may influence tumor proliferation and survival by modulating energy metabolism pathways.

Given the strong association between histidine metabolism and liver cancer, targeting enzymes involved in histidine metabolism or its downstream products has become a research focus. For instance, inhibiting histidine decarboxylase or blocking histamine receptor activity may prevent pro-tumor signaling in the tumor microenvironment [13, 33–36]. Moreover, modulating tumor cell metabolic pathways, such as oxidative stress or energy metabolism, could provide novel avenues for liver cancer treatment. Histidine metabolism plays a complex and multifaceted role in the onset and progression of liver cancer, influencing tumor cell behavior through pathways involving inflammation, immunity, oxidative stress, and energy metabolism. Consequently, further research into the mechanisms by which histidine metabolism affects liver cancer, as well as exploration of targeted therapeutic strategies for histidine metabolic pathways, may offer new directions and opportunities for early intervention and treatment.

Through an in-depth analysis of single-cell sequencing data from liver cancer coupled with both in vivo

and in vitro experiments, we found that histidine metabolism promotes tumor development and affects patient prognosis by reprogramming tumor cell metabolism, modulating the immune microenvironment, and inhibiting immune cell infiltration. Furthermore, we constructed a prognostic model based on histidine metabolism and identified the gene BUD23 as having the most significant influence on tumor progression. This gene may serve as a biomarker for clinical detection and prediction of immunotherapy efficacy.

Methods and materials

Databases and software

The HCC scRNA-seq datasets were downloaded from the GEO database (www.ncbi.nlm.nih.gov/geo/), including GSE149614. RNA-seq gene expression data of patients with LIHC and the clinical information of the patients were downloaded from the UCSC XENA Data Portal (https://xena.ucsc.edu). Level 3 data of LIHC patients were obtained from Xiantao Academe (https://www.xiantaozi.com), which included relevant clinical data and survival information. The UALCAN tool, available through the University of Alabama at Birmingham Cancer Data Analysis Portal(http://ualcan.path.uab.edu), was used for translational, proteomic, and clinical correlation analyses. The scRNA-seq dataset analysis was performed using Seurat (v4.4.1) in R. First, the two large scRNA-seq datasets were integrated and batch-corrected using the "IntegrateData" function. Cells that did not meet the quality control criteria (200 < nFeature RNA < 8000, and percent.mt < 15%) were subsequently excluded from the integrated dataset. Standard Seurat workflows were then applied, including t-distributed stochastic neighbor embedding(t-SNE). Furthermore, the "Harmony" R package (https://github.com/immunogenomics/harmony) was used to integrate gene-cell matrices from different samples. Cluster-specific genes were annotated by matching them with previously reported cell population features in the CellMarker database.

Cell culture

The hepG2 and THP-1 cell line used in this study was obtained from Procell and verified to be free of mycoplasma contamination. The general procedure for maintaining these cell cultures has been described previously. Briefly, the cells were cultured in DMEM high-glucose or RPMI 1640 medium supplemented with 10% fetal bovine serum (FBS, Procell) and maintained in a humidified incubator at 37 °C with 5% CO_2.

Antibodies and chemicals

Antibodies(chemicals)	Source	Identifier
FITC anti-human CD11b	Biolegend	301,330
PE anti-human CD86	Biolegend	305,438
APC anti-human CD163	Biolegend	333,610
Purified NA/LE Hamster Anti-Mouse CD3e	BD Pharmingen	553,057
Purified NA/LE Hamster Anti-Mouse CD28	BD Pharmingen	553,294
PerCP/Cyanine5.5 anti-mouse CD3	Biolegend	100,218
APC anti-mouse CD4	Biolegend	100,412
FITC anti-mouse CD8a	Biolegend	100,706
PE anti-mouse CD279	Biolegend	135,205
PE anti-mouse CD69	Biolegend	104,507
APC/Fire™ 750 anti-mouse CD45	Biolegend	103,154
PE/Cyanine7 anti-mouse F4/80	Biolegend	123,114
FITC anti-mouse CD11b	Biolegend	101,206
PE anti-mouse CD206	Biolegend	141,706
PE anti-mouse CD86	Biolegend	105,008
APC anti-mouse CD80	Biolegend	104,714
APC anti-mouse CD163	Biolegend	155,306
PE anti-mouse I-A/I-E	Biolegend	107,608
PE anti-mouse H2Kb	BD Pharmingen	561,072
PE anti-mouse TNF-α	Biolegend	506,306
PE anti-mouse CD274	Biolegend	124,308
PE anti-mouse IFN-γ	Biolegend	505,807
CD3 Monoclonal Antibody	eBioscience	16-0037-81
CD28 Monoclonal Antibody	eBioscience	16-0289-81
PerCP/Cyanine5.5 anti-human CD3	Biolegend	317,335
APC anti-human CD4	Biolegend	300,514
FITC anti-human CD8a	Biolegend	300,905
PE anti-human CD279	Biolegend	329,905
PE anti-human CD69	Biolegend	310,905
WBSCR22 Polyclonal antibody	Proteintech	28192-1-AP
HRP-conjugated Alpha Tubulin Recombinant antibody	Proteintech	HRP-80,762
PMA	Solarbio	P6741
L-Histidine	Solarbio	H0020
Lipofectamine 3000	Invitrogen	L3000015

Cell transfection

Small interfering RNAs (siRNAs) for downregulation of target genes were constructed by Hanyibio (Guangzhou, China). Briefly, indicated cells (1×10^5 cells) were seeded into 6-well plates and cultured overnight to a confluence of approximately 70%. Subsequently, cells were transfected with indicated siRNAs using a Lipofectamine 3000 kit (Invitrogen, Waltham, MA, USA). Downregulation of target genes was confirmed using RNA extraction and qRT-PCR analysis.

Name	Sequences
siAOC-1	UAGAACUUCCCGUUGUACCAC GGUACAACGGGAAGUUCUAUG
siAOC-2	UGGUAUUGAGGAAGAACUGAU CAGUUCUUCCUCAAUACCACA
siBUD23-1	UAUUCUCUGGCAGAUAAAGAA CUUUAUCUGCCAGAGAAUAAG
siBUD23-2	UCUUGUUAGCAUUACAGAGCC CUCUGUAAUGCUAACAAGAAG

RNA extraction and qRT-PCR analysis

According to the manufacturer's instructions, total RNA was isolated from cultured cell samples using the EZpress RNA Purification Kit (EZBioscience, B0004). cDNA was then synthesized using the PrimeScript RT Kit (TaKaRa Bio, RR036A), followed by qRT-PCR using the SYBR Green PCR Master Mix (Life Technologies, A25742). ACTB was used as an endogenous reference for the quantification and normalization of PCR products.

Primer name[a]	Primer sequence
ACTB-F	CACCATTGGCAATGAGCGGTTC
ACTB-R	AGGTCTTTGCGGATGTCCACGT
AOC1-F	TACGTCCACGCCACCTTCTACA
AOC1-R	GTCTGGAAGCTGTTCTTGGTGC
BUD23-F	ATGAGGCTGTGGACCGAGAGAT
BUD23-R	TACAGAGCCACTGCACAGCAGA

a: F, forward primer; R, reverse primer

Western blot

Cells were lysed in RIPA Lysis Buffer (Beyotime, P0013C) at 4 °C for 30 min, with vortexing every 5 min. The lysate was centrifuged at 13,000 × g for 20 min at 4 °C, and the supernatant was collected for protein concentration measurement using the BCA assay. SDS-PAGE Sample Loading Buffer (Beyotime, P0015) was added, and proteins were denatured at 100 °C for 10 min. Proteins were then separated using 10% SDS-PAGE and transferred onto a PVDF membrane (Millipore, USA). The membrane was blocked with 5% milk for 1 h and incubated with the primary antibody overnight at 4 °C. Finally, after incubation with the secondary antibody (Proteintech, SA00001-2), protein bands were visualized using a chemiluminescence imaging system (LAS500).

Seahorse XF analysis

The XF96 sensor cartridge was hydrated overnight in a 37 °C non-CO_2 incubator with Seahorse XF calibration solution (#103095-000, Agilent). HepG2 cells were seeded into a Seahorse XF96 cell culture microplate (Agilent, CA, USA) at a density of 1×10^4 cells per well and cultured for 48 h with or without 30 mM histidine. Alternatively, HepG2 cells transfected with siRNAs were seeded into a Seahorse XF96 cell culture microplate at a density of 2×10^4 cells per well and cultured for 24 h.

For the mitochondrial stress test, cells were washed and incubated in Seahorse XF basal medium supplemented with glucose (10 mM), pyruvate (1 mM), and glutamine (2 mM) in a 37 °C non-CO_2 incubator for 1 h. The oxygen consumption rate (OCR) was monitored while sequentially adding 2 μM oligomycin, 1 μM FCCP, and 0.5 μM rotenone/antimycin A (from the Seahorse XF Cell Mito Stress Test Kit, #103015-100, Agilent) to assess mitochondrial respiratory capacity. The Seahorse XF96 analyzer (Agilent, CA, USA) was used to measure extracellular acidification rate (ECAR) and OCR according to the manufacturer's instructions.

For the glycolytic rate assay, cells were washed and incubated in Seahorse XF basal medium supplemented with glucose (10 mM), pyruvate (1 mM), and glutamine (2 mM) in a 37 °C non-CO_2 incubator for 1 h. ECAR was monitored while sequentially adding 0.5 μM Rot/AA and 50 mM 2-DG from the Seahorse XF Glycolytic Rate Assay Kit (#103344-100, Agilent) to assess glycolytic capacity. The Seahorse XF96 analyzer (Agilent, CA, USA) was used to measure ECAR and OCR according to the manufacturer's instructions. Data analysis and report generation were performed using Seahorse Analytics.

Hematoxylin and Eosin staining and immunohistochemistry analysis

After euthanizing the mice, the tumor tissues were immediately fixed in 4% paraformaldehyde. Hematoxylin and eosin (HE) staining and immunohistochemical staining were performed by Wuhan Servicebio Technology Co., Ltd. Tissue sections were imaged at room temperature using a Pannoramic MIDI digital slide scanner (3DHISTECH). Images were analyzed using QuPath software.

Immunohistofluorescence staining

After euthanizing the mice, the tumor tissues were immediately fixed in 4% paraformaldehyde. Immunohistofluorescence staining were performed by Wuhan BaiQianDu bio Technology Co., Ltd. The tissue sections were imaged at room temperature using a Pannoramic SCAN digital slide scanner (3DHISTECH). Images were analyzed using CaseViewer and ImageJ software.

In vitro macrophage polarization assay

HepG2 cells were treated with various concentrations of histidine for 48 h or transfected with siRNA, after which the conditioned medium was collected.

THP-1 cells were cultured in RPMI-1640 medium supplemented with 10% fetal bovine serum (FBS) and 1% penicillin/streptomycin at 37 °C in a 5% CO_2 atmosphere. When cell density reached 80%, phorbol 12-myristate 13-acetate (PMA, 50 ng/mL) was used to induce differentiation into M0 macrophages for 24 h. The cells were then washed with PBS, and conditioned medium were added. The cells were cultured at 37 °C with 5% CO_2 for an additional 48 h. Subsequently, cells were then collected, stained, and labeled, and the expression levels of CD86 and CD163 were measured using flow cytometry.

In vitro T cell differentiation and functional assay

Hepa1-6 cells were treated with various concentrations of histidine for 48 h or, in the case of HepG2 cells, subjected to siRNA transfection before collecting the conditioned medium. Mice were euthanized, and spleens were collected. The spleens were minced and filtered to obtain a single-cell suspension. Lymphocytes were isolated using a lymphocyte separation medium, followed by red blood cell lysis and washed with PBS. Human peripheral blood lymphocytes were similarly isolated using a lymphocyte separation reagent, with red blood cells removed and the remaining cells washed with PBS. The isolated lymphocytes were seeded into culture dishes pre-coated overnight with CD3 antibodies and cultured at 37 °C with 5% CO_2 in a medium containing CD28 and conditioned medium for 48 h. Subsequently, the cells were then collected, stained, and labeled, lymphocyte differentiation, activation, and exhaustion were measured using flow cytometry.

Mouse subcutaneous tumor model

Four-week-old male C57BL/6 mice were selected, and 10^6 Hepa1-6 cells were injected subcutaneously. The drinking water of the treatment group was replaced with a 100 mM histidine aqueous solution, and tumor volume was measured every 5 days starting on Day 7. After 22 days, tumors were collected, and single-cell suspensions were prepared for subsequent lymphocyte isolation. The cell suspensions were stained and labeled, and immune cell infiltration, macrophage polarization and function, as well as lymphocyte differentiation, activation, and exhaustion, were measured using flow cytometry.

Mouse liver orthotopic tumor model

Four-week-old male C57BL/6 mice were selected, and 10^6 Hepa1-6-luc cells were injected into the liver via laparotomy. Starting on day 7 post-injection, the luciferase signals in the mice were monitored every 5 days using an in vivo imaging system to track tumor growth. On day 22, livers were collected and fixed in paraformaldehyde to prepare paraffin-embedded sections. Immunofluorescence was performed to assess immune cell infiltration, macrophage polarization and function, as well as lymphocyte differentiation, activation, and exhaustion levels.

Statistical analysis

All statistical analyses were performed using GraphPad Prism (version 9.4.1) and R software. Data were presented as mean ± standard deviation (SD) unless otherwise specified. The normality of the data distribution was assessed using the Shapiro-Wilk test. For comparisons between two groups, an unpaired two-tailed Student's t-test was applied if the data were normally distributed, otherwise, the Mann-Whitney U test was used for non-parametric data. For comparisons among multiple groups, one-way analysis of variance (ANOVA) followed by Tukey's post-hoc test was used for parametric data, whereas the Kruskal-Wallis test followed by Dunn's post-hoc test was used for non-parametric data. Kaplan-Meier survival curves were generated to analyze overall survival, and statistical differences were determined using the log-rank (Mantel-Cox) test. Correlation analyses were conducted using Pearson's correlation for normally distributed variables and Spearman's rank correlation for non-parametric data. *P*-values less than 0.05 were considered statistically significant. All experiments were performed in triplicate or more to ensure reproducibility. Statistical significance is indicated in the figures by $^{*}P < 0.05$, $^{**}P < 0.01$, $^{***}P < 0.001$. Data visualization, including box plots, bar charts, and scatter plots, was generated using GraphPad Prism to illustrate key findings clearly and effectively.

Results

Single-cell sequencing analysis revealed the comprehensive regulatory impact of histidine metabolism on the tumor immune microenvironment

To investigate the global regulation of histidine metabolism on the tumor microenvironment, we downloaded single-cell sequencing data of HCC from the GEO database. Following quality control, a total of 32,984 high-quality cells were obtained. A list of histidine metabolism-related genes was retrieved from the GSEA database. Cell metabolic scores were calculated using the AUCell algorithm and grouped into His-HIGH and His-LOW categories. These cells were clustered into 41 clusters using t-SNE (Fig. 1A). The expression profiles of marker genes in different cell clusters were analyzed (Supplementary Fig. 1A). Through systematic annotation strategies, six major cell types were identified, including hepatocytes, T/

NK cells, B cells, macrophages, endothelial cells, and fibroblasts (Fig. 1B). Based on the annotation results, we verified the high expression of marker genes in the corresponding cell types: hepatocytes exhibited high expression levels of ALB, EPCAM, HNF4A, and SERPINA1, macrophages exhibited high expression levels of CD14, CD68, CD86, CD163, IL1B, and LYZ, T/NK cells expressed high levels of CD3D, CD3E, IL7R, and NKG7, B cells exhibited high expression levels of CD79A, IGHG1, and JCHAIN, endothelial cells exhibited high expression levels of Pecam1 and VWF, fibroblasts exhibited high expression levels of ACTA2 and Col1a1 (Supplementary Fig. 1B). Analysis of cell proportions revealed that hepatocytes were more abundant in high histidine metabolism group, whereas immune and stromal cells were less prevalent (Fig. 1C, D). Differential expression analysis showed that histidine metabolism-related genes were highly expressed in hepatocytes, moderately expressed in macrophages, and minimally expressed in lymphocytes and stromal cells (Supplementary Fig. 1C). Altogether, these findings indicate that elevated histidine metabolism is associated with an expansion of liver cancer cells and a reduction in immune and stromal cell infiltration within the tumor microenvironment.

We analyzed intercellular interactions to determine how histidine metabolism influences cell communication networks. Our findings revealed a marked decrease in both the number and intensity of interactions among various cell types in the high histidine metabolism group. This decrease was most pronounced in the crosstalk between stromal and immune cells, although reduced communication between parenchymal cells and both immune and stromal cells was also evident (Fig. 1E, F, Supplementary Fig. 1D, E). Further investigation showed significant downregulation in cell-to-cell interactions mediated by parenchymal cells—particularly through the MIF, FN1, MK, SPP1, VTN, and PARs signaling axes targeting themselves, immune cells, or stromal cells (Fig. 1G). Moreover, GSVA analysis indicated that pathways related to immune responses and immune cell activation were less enriched in the high histidine metabolism group, whereas oxidative phosphorylation pathways were more enriched (Fig. 1H).

In summary, histidine metabolism regulates cell-cell interactions to inhibit immune cell infiltration and immune response.

Elevated histidine metabolism inhibits immune cell infiltration by metabolically reprogramming tumor cells and stromal cells

To investigate the ecological impact of histidine metabolism on different cell types within the immune microenvironment, we reclustered hepatocytes using t-SNE, identifying 18 main clusters that were subsequently divided into high and low histidine metabolism groups (Fig. 1I, Supplementary Fig. 2A). KEGG enrichment analysis of gene expression in these two groups revealed a significant upregulation of genes involved in diverse metabolic processes (Fig. 1J), whereas genes associated with proliferation, migration, and invasion—the defining characteristics of malignancy—did not show substantial changes (Fig. 1K). To validate these analytical results, we conducted Seahorse metabolic analysis on human hepatocellular carcinoma cell lines. Consistent with previous findings, histidine treatment led to an increase in ATP-linked respiration and enhanced oxidative phosphorylation (Fig. 1L, Supplementary Fig. 2B). Meanwhile, the glycolytic rate of the cells was also elevated (Fig. 1M, Supplementary Fig. 2C). t-SNE analyses of various metabolic pathways demonstrated an activation of lipid, glucose, and amino acid metabolism in parenchymal cells with high histidine metabolism, consistent with earlier GSVA findings (Supplementary Fig. 2D).

We further examined TCGA data by scoring histidine metabolism gene sets and dividing samples into high and low histidine metabolism groups. Using both the SSGSEA and xCell algorithms, we assessed the impact of histidine metabolism on immune cell infiltration. Across different analytical methods, the results consistently showed lower immune cell infiltration in the high histidine metabolism group (Fig. 1N, Supplementary Fig. 2E). GSEA also indicated that histidine metabolism was negatively correlated with immune activation pathways (Fig. 1O).

From these findings, we infer that histidine metabolism does not directly influence tumor proliferation but instead reshapes the tumor microenvironment by altering tumor cells metabolism and modulating interactions between tumor cells, immune cells, and stromal cells, ultimately creating a microenvironment more conducive to tumor growth.

Fibroblasts play a crucial role in cell communication and contribute significantly to the formation of the tumor microenvironment. Therefore, we further analyzed fibroblasts. Clustering analysis identified eight major fibroblast subpopulations (Supplementary Fig. 3A). Systematic annotation based on gene expression profiles revealed three key subtypes: my-ACTA2 + CAFs (myofibroblast-like CAFs), mat-POSTN + CAFs (matrix-producing CAFs), and pro-C7 + CAFs (pro-inflammatory CAFs) (Supplementary Fig. 3B, C).

By analyzing the differential expression of histidine metabolism-related genes and performing UMAP analysis of marker genes, we found that the infiltration

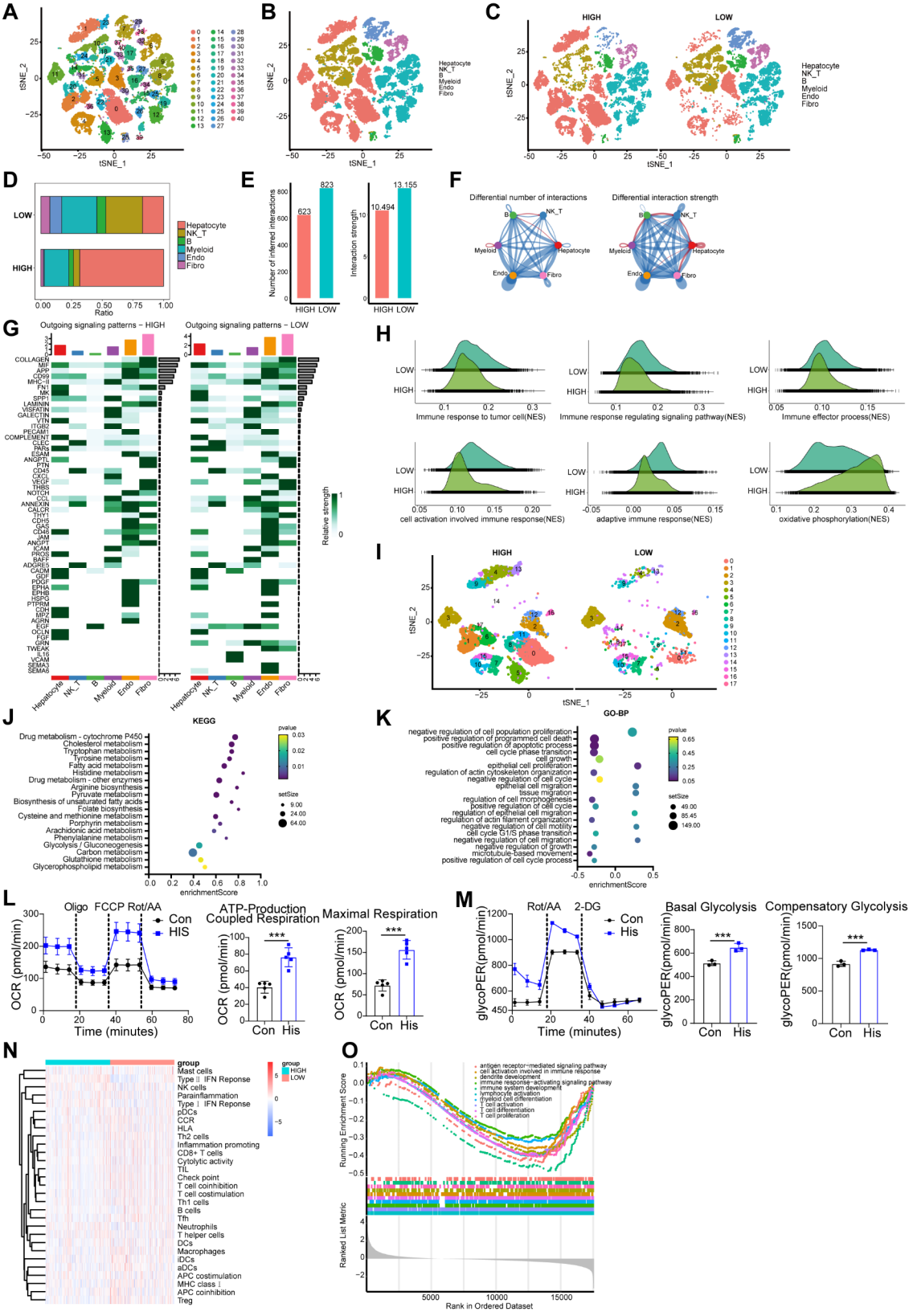

Fig. 1 (See legend on next page.)

(See figure on previous page.)

Fig. 1 Single-cell sequencing analysis revealed global regulatory effect of histidine metabolism on tumor immune microenvironment. (**A**) t-SNE plot displaying eight liver cancer single-cell datasets clustered into 41 distinct cell clusters via dimensional reduction. (**B**) Annotation based on marker gene expression classified the cells into six groups: hepatocytes, macrophages, T cells, B cells, endothelial cells, and fibroblasts. (**C**) t-SNE plot dividing cells into two groups based on histidine metabolism levels: high histidine metabolism group(left) and low histidine metabolism group(right). (**D**) Proportions of each cell type within the high and low histidine metabolism groups. (**E**) Quantitative analysis of intercellular interactions ranked by interaction frequency and strength. (**F**) Network diagram illustrating how histidine metabolism affects intercellular interactions. Blue nodes indicate downregulated interactions in the high histidine metabolism group, and red nodes indicate upregulated ones. (**G**) Heatmap depicting the intensity of signaling axes across cell interactions in the high (left) and low (right) histidine metabolism groups (e.g., MIF, CLEC, MHC II, SPP1). (**H**) Ridge plot of GSVA analysis showing pathway enrichment in the high and low histidine metabolism groups. (**K**) t-SNE plot displaying hepatocytes clustered into 18 cell clusters via dimensional reduction. (**I**) Division of hepatocytes into two groups based on histidine metabolism levels. (**J**) Bubble plot displaying the results of KEGG enrichment analysis on the impact of histidine metabolism on hepatocyte functions. (**N**) Bubble plot displaying the results of GO enrichment analysis on the impact of histidine metabolism on hepatocyte functions. (**L**) Seahorse analysis of the impact of histidine on oxygen consumption rate (OCR). (**M**) Seahorse analysis of the impact of histidine on glycolytic rate (glycoPER). (**N**) Heatmap (SSGSEA) analyzing the impact of histidine metabolism on immune infiltration in HCC samples from the TCGA database. (**O**) GSEA results showing the effect of histidine metabolism on immune-related pathways in TCGA HCC data. Error bars represent the SD obtained from five or three independent experiments; ***$P < 0.001$。

of all three CAF subtypes was reduced in the high histidine metabolism group (Supplementary Fig. 3D, E). GSVA analysis further demonstrated that high histidine metabolism significantly downregulated fibroblast-mediated immune responses (Supplementary Fig. 3F, G), with the most pronounced suppression observed in pro-C7 + CAFs (Supplementary Fig. 3H). Additionally, KEGG and GO enrichment analyses revealed upregulation of multiple metabolism-related pathways in fibroblasts (Supplementary Fig. 3I, J). Based on these findings, we hypothesize that histidine metabolism regulates fibroblast metabolic reprogramming, modulating cell communication to suppress immune responses.

In summary, we propose that high histidine metabolism reprograms the metabolism of both tumor and stromal cells, influencing cell communication, inhibiting immune cell infiltration, and reshaping the tumor microenvironment, thereby promoting tumor progression.

Elevated histidine metabolism suppresses the antitumor activity of macrophages

In recent years, the crosstalk between tumor cell metabolism and the immune microenvironment has garnered increasingly attention for its role in tumorigenesis and progression [16, 37, 38]. To investigate the impact of elevated histidine metabolism on the immune microenvironment, we reclustered macrophages, resulting in 16 primary cell clusters (Fig. 2A). Systematic annotation based on gene expression profiles of each cluster, we identified several macrophage subtypes, including IFN-ISG15 + macrophages (interferon-related macrophages), HSP-HSP + macrophages (heat shock protein-related macrophages), LA-APO + macrophages (lipid-associated macrophages), Angio-VCAN + macrophages (angiogenesis-related macrophages), RTM-MARCO + macrophages (tissue-resident macrophages), and Inflam-AREG + macrophages (inflammation-related macrophages) (Fig. 2B, Supplementary Fig. 4A, B).

We next examined the differential expression of histidine metabolism–related genes. In the high histidine metabolism group, the number of macrophages with antitumor functions, such as HSP-HSP + macrophages and Inflam-AREG + macrophages, was significantly reduced. Conversely, the number of macrophages lacking antitumor functions or exhibiting immunosuppressive properties, such as LA-APO + macrophages and RTM-MARCO + macrophages, increased (Fig. 2 C, D). The accuracy of these annotations was further validated through t-SNE expression analysis of marker genes (Supplementary Fig. 4C).

To investigate the impact of histidine metabolism on macrophage function, enrichment analyses revealed that histidine metabolism upregulated the expression of genes associated with various metabolic processes in macrophages, while inhibiting their antitumor activities such as cell–cell communication, signal transduction, cell proliferation, cytokine production, and responses to cytokines (Fig. 2E, F). We further explored how histidine metabolism shapes macrophage-mediated intercellular communication by performing CellChat analysis of interactions between macrophages and other cell types. The ADGRE5, ANNEXIN, EGF, CLEC, CALCR, and CXCL signaling axes were significantly downregulated in macrophage–macrophage, macrophage–immune cell, or macrophage–stromal cell crosstalk (Fig. 2G). Next, we investigated changes in different macrophage subpopulations. GSVA analysis showed that in the high histidine metabolism group, macrophage activation, chemotaxis, immune responses, cytokine production and signaling, and antigen presentation pathways were markedly downregulated—especially in HSP-HSP$^+$ macrophages and Inflam-AREG$^+$ macrophages, both of which display antitumor properties (Fig. 2H). These findings suggest that in an immune microenvironment characterized by elevated histidine metabolism,

macrophage antitumor function is substantially diminished.

Additionally, we performed in vitro co-culture experiments using THP-1–derived M0 macrophages to examine how variations in histidine metabolism affect macrophage polarization (Fig. 2I). With increasing histidine concentrations, macrophages showed a tendency to differentiate more toward the M2 phenotype, while differentiation into M1-type macrophages, which possess antitumor properties, was significantly reduced. These results further illustrate that histidine metabolism drives metabolic reprogramming in tumor cells, modifies macrophage differentiation through intercellular signaling, and ultimately reshapes macrophage function and the tumor microenvironment, thereby promoting tumor progression.

Elevated histidine metabolism suppresses the antitumor activity of T cells

We performed clustering analysis on another important immune cell population, NK_T cells, and identified two subpopulations: NK cells and T cells (Supplementary Fig. 5A). To investigate the effect of elevated histidine metabolism on the antitumor function of T cells, we reclustered T cells and identified 12 primary cell clusters (Fig. 3A). Based on the gene expression profiles of each cluster, we performed systematic annotation and identified several T cells subtypes, including Tem-GZMA + cells (effector memory T cells), Tn-CCR7 + cells (naive T cells), HSP-T-HSP + cells (T cells expressing multiple heat shock proteins), Treg-Ctla4 + cells (regulatory T cells), and Trm-CD69 + cells (tissue-resident memory T cells) (Fig. 3B, Supplementary Fig. 5B, C). Further t-SNE expression analysis of marker genes confirmed the accuracy of these annotations (Supplementary Fig. 5D). The results demonstrated that in the high histidine metabolism group, T cell infiltration was reduced, and the proportion of T cells lacking antitumor function or exhibiting immunosuppressive properties increased, including Trm-Cd69 + cells, Treg-Ctla4 + cells, and Tn-CCR7 + cells. Conversely, the proportion of T cells with antitumor functions, such as Tem-GZMA + cells and HSP-T-HSP + cells, was decreased (Fig. 3 C, D).

To investigate how histidine metabolism impacts T-cell crosstalk, we utilized CellChat to analyze cell-cell interactions among various T cell subpopulations, finding particularly strong connections between Tem-GZMA + cells, Treg-Ctla4 + cells, and HSP-T-HSP + cells (Supplementary Fig. 5E). Further analyses revealed that signaling axes such as CLEC, MIF, MHC II, CD99, and SPP1—targeting Tem-GZMA$^+$ cells via Treg-Ctla4$^+$ or HSP-T-HSP$^+$ cells—played pivotal roles in T-cell interactions (Fig. 3E). In the high histidine metabolism group, these axes (CLEC, MIF, SPP1, MHC II) were all notably downregulated in T cells' interactions with other cells or among themselves (Fig. 3F).

We also conducted GSEA on different T-cell subsets. In the high histidine metabolism group, antitumor functions—including activation, chemotaxis, proliferation, and cytokine production—were markedly suppressed in Tem-GZMA$^+$ and HSP-T-HSP$^+$ cells, Trm-CD69$^+$ cells also showed a certain degree of downregulation (Fig. 3G). Meanwhile, GO enrichment analysis revealed that high histidine metabolism suppressed T cell gene expression, transcription, and activation functions (Fig. 3H). Taken together, these findings suggest that in an immune microenvironment characterized by elevated histidine metabolism, these signaling axes modulate T-cell activation, migration, and cytokine production, reshaping the immune microenvironment to favor tumor progression.

We also isolated splenic lymphocytes from mice and conducted in vitro co-culture experiments to investigate how different levels of histidine metabolism affect T-cell function (Fig. 3I). As histidine concentration increased, the proportion of T cells differentiating into CD4$^+$ and CD8$^+$ subtypes decreased, while the fraction of CD4$^+$PD1$^+$ and CD8$^+$PD1$^+$ T cells rose. This shift indicates enhanced T-cell exhaustion. Additionally, CD69 expression on both CD4$^+$ and CD8$^+$ T cells declined, reflecting lower activation levels (Fig. 3J, Supplementary Fig. 5F, G, H). These findings suggest that heightened histidine metabolism suppresses T-cell differentiation and activation while promoting exhaustion, ultimately altering the tumor microenvironment to favor tumor progression.

Collectively, these results indicate that histidine metabolism reshapes the tumor microenvironment by regulating T-cell differentiation, suppressing activation, and driving exhaustion, thereby promoting tumor progression.

Elevated histidine metabolism suppresses the antitumor activity of NK cells

Natural killer (NK) cells are a key component of immune cells in the tumor microenvironment. Therefore, we performed clustering analysis on NK cells (Supplementary Fig. 6A). The results showed that in the high histidine metabolism group, NK cell infiltration was significantly reduced (Supplementary Fig. 6B), and NK cell functions, including cell activation, cytotoxicity, and cytokine production, were weakened. Additionally, NK cell-mediated immune responses were downregulated (Supplementary Fig. 6C). This further supports our hypothesis that histidine metabolism reshapes the immune microenvironment by

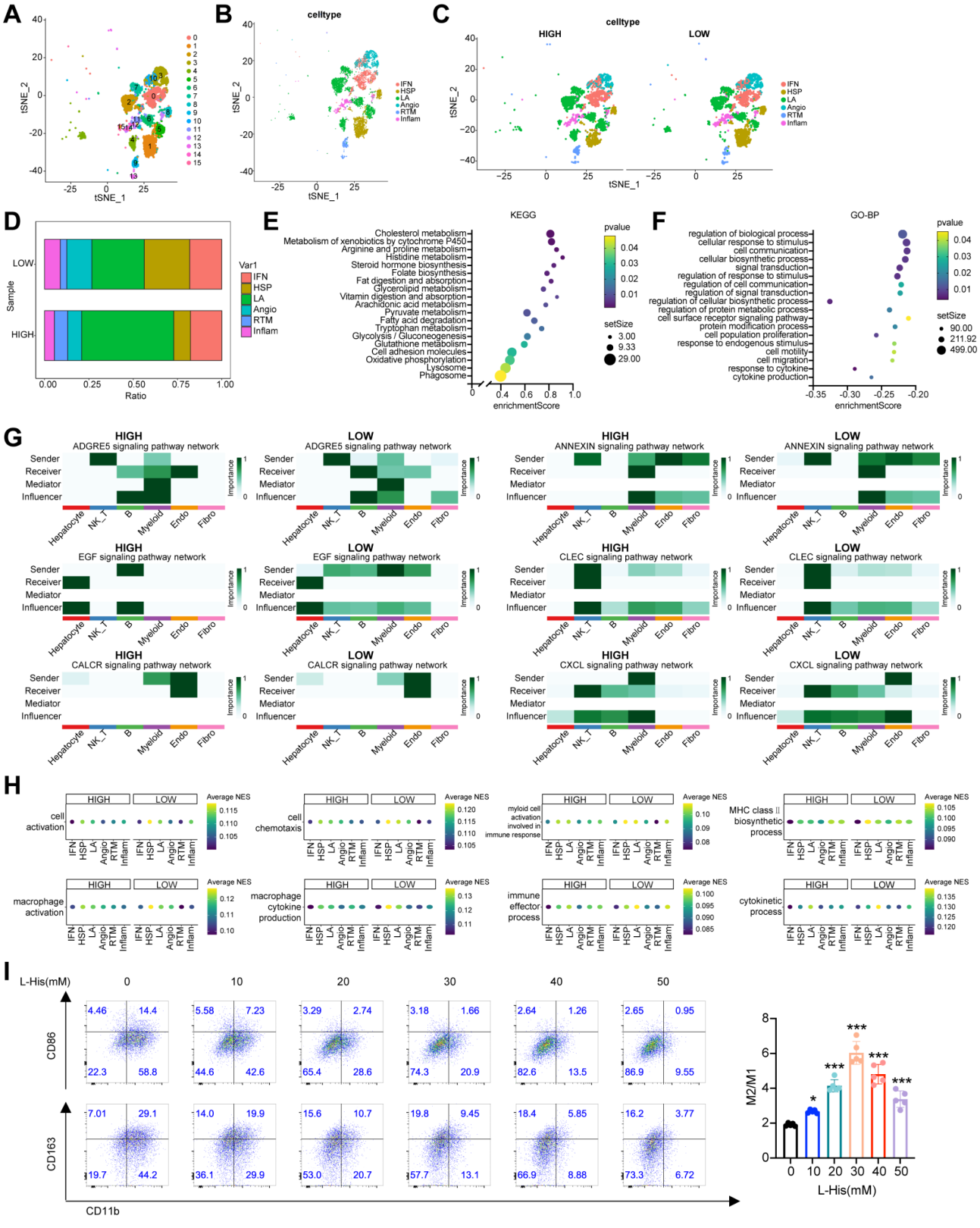

Fig. 2 (See legend on next page.)

(See figure on previous page.)

Fig. 2 High Histidine Metabolism Suppresses the Antitumor Function of Macrophages. (**A**) t-SNE plot displaying macrophages clustered into 16 distinct cell clusters via dimensional reduction. (**B**) Annotation based on marker gene expression classified macrophages into six subpopulations: IFN-ISG15 + macrophages, HSP-HSP + macrophages, LA-APO + macrophages, Angio-VCAN + macrophages, RTM-MARCO + macrophages, and Inflam-AREG + macrophages. (**C**) Bubble chart displaying the expression of marker genes in each macrophage subpopulation. (**D**) t-SNE plot dividing macrophages into two groups based on histidine metabolism levels: high histidine metabolism group(left) and low histidine metabolism group(right). (**E**) Bubble chart of KEGG enrichment results indicating how histidine metabolism affects macrophage function. (**F**) Bubble chart of GO enrichment results illustrating the influence of histidine metabolism on macrophage function. (**G**) Heatmap of intercellular communication intensities for signaling axes such as ADGRE5, ANNEXIN, EGF, CLEC, CALCR, and CXCL across the high and low histidine metabolism groups. (**H**) Bubble chart (GSEA) of functional pathway enrichment in macrophage subpopulations in high vs. low histidine metabolism conditions. (**I**) Representative flow cytometry pseudocolor plots showing the polarization of THP-1–derived M0 macrophages after treatment with varying concentrations of histidine. The right panel shows the quantification. Error bars represent the SD from five independent experiments, $^{*}P < 0.05$, $^{***}P < 0.001$

inhibiting the functions of various immune cells, thereby promoting tumor progression.

Elevated histidine metabolism promotes tumor growth in mice by modulating the tumor microenvironment

To verify whether elevated histidine metabolism affects tumor growth in vivo, we established a subcutaneous liver tumor model in mice. By providing additional dietary histidine, we constructed a high histidine metabolism model (Fig. 4A). Tumor measurements showed that the tumor proliferation rate in the high histidine treatment group was significantly faster, with noticeably larger tumor volumes (Fig. 4B-D).

Flow cytometric analysis of cells extracted from the subcutaneous tumor tissue revealed that the proportion of CD45 + immune cells infiltrating the tumors in the high histidine treatment group was significantly reduced (Fig. 4E).

Notably, the fraction of $CD11b^{+}F4/80^{+}$ macrophages as well as $CD11b^{+}F4/80^{-}$ cells increased (Fig. 4F). However, among macrophages, only the non-antitumor $CD80^{+}CD86^{+}$ (M1 phenotype) subset significantly expanded in the high histidine–treated tumors, whereas $CD163^{+}CD206^{+}$ (M2 phenotype) macrophages with antitumor characteristics showed a slight decrease (Fig. 4G, Supplementary Fig. 7A). Additionally, the proportion and fluorescence intensity of $TNF\alpha^{+}$ macrophages rose, as did $PD\text{-}L1^{+}$ fluorescence intensity, indicating weakened antitumor activity. Macrophages expressing the antigen presentation molecules $I\text{-}A/I\text{-}B^{+}$ and $H2Kb^{+}$ showed reduced fluorescence intensity, especially in the $H2Kb^{+}$ subset, suggesting compromised antigen presentation (Fig. 4G, Supplementary Fig. 7B, C).

In lymphocytes, the proportions of infiltrating CD4 + T cells and CD8 + T cells in the tumors of the high histidine treatment group were significantly reduced (Fig. 4H, Supplementary Fig. 7D). We further assessed $CD4^{+}$ and $CD8^{+}$ T-cell function: both subtypes exhibited decreased frequencies of activated ($CD69^{+}$) T cells, and their mean fluorescence intensity for CD69 also declined, indicating reduced activation. The proportion of cytotoxic ($GZMB^{+}$, $TNF\alpha^{+}$, $IFN\gamma^{+}$) T cells dropped notably, along with decreased mean fluorescence intensities for these markers, signifying compromised T-cell killing activity. Meanwhile, $PD1^{+}$ T cells were more abundant, and their mean fluorescence intensity for PD1 increased—both hallmark indicators of heightened T-cell exhaustion (Fig. 4I, Supplementary Fig. 7E). These in vivo experiments further confirm our earlier conclusion that elevated histidine metabolism promotes tumor progression by modulating the tumor microenvironment, inhibiting immune cell infiltration, and impairing immune function.

Given the potential differences between the immune microenvironment of subcutaneous tumors and liver tumors, we established a liver orthotopic tumor model in mice. Again, additional dietary histidine was used to induce a high histidine metabolism state. Consistent with previous findings, tumors in the high histidine treatment group exhibited significantly faster proliferation, resulting in noticeably larger tumor volumes (Fig. 4J, K). There was no significant change in the body weight of the mice (Supplementary Fig. 8A). Histological analysis using HE staining and immunohistochemistry revealed that histidine treatment did not affect the proliferation of tumor cells in liver orthotopic tumors (Fig. 4L, Supplementary Fig. 8B, C). Immunofluorescence analysis indicated that, in the high histidine treatment group, infiltration of CD8 + T cell into the tumors was reduced, while the number of PD1 + T cells increased, leading to elevated T cell exhaustion. Additionally, the number of GZMB + T cells decreased, further suggesting impaired antitumor functionality (Fig. 4M, Supplementary Fig. 8D). Similarly, macrophage infiltration was decreased in the high histidine treatment group. Specifically, the infiltration of CD86 + M1 macrophages was reduced, H2D1 expression was downregulated, and macrophage antitumor function was impaired (Fig. 4N, Supplementary Fig. 8E). The liver orthotopic tumor experiment further demonstrated that histidine metabolism promotes tumor growth not by directly affecting tumor cell proliferation, but by suppressing immune cell infiltration and function.

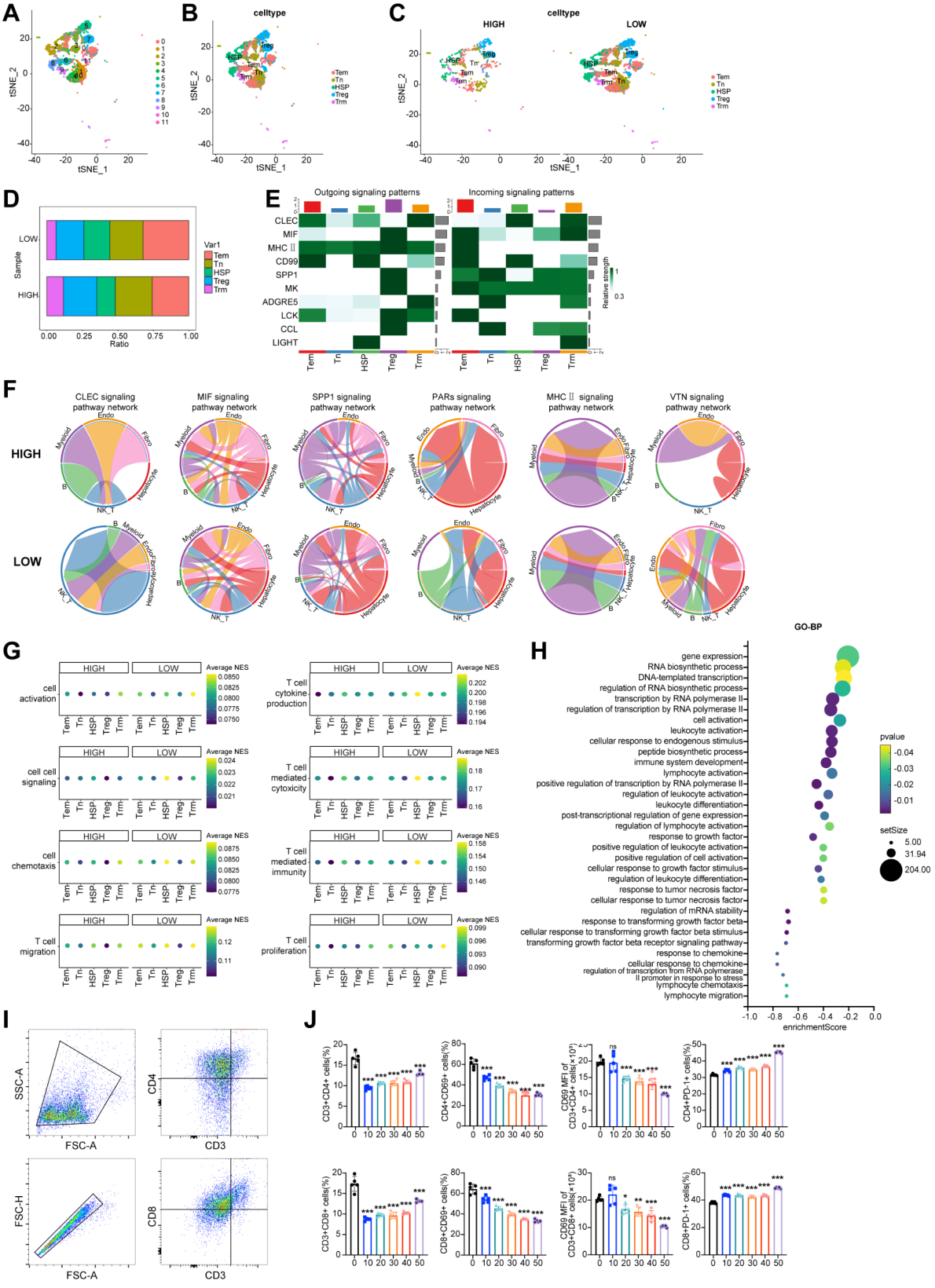

Fig. 3 (See legend on next page.)

(See figure on previous page.)

Fig. 3 High Histidine Metabolism Suppresses the Antitumor Function of T Cells. (**A**) t-SNE plot displaying T cells clustered into 12 distinct cell clusters via dimensional reduction. (**B**) Annotation based on marker gene expression classified T cells into five subpopulations: Tem-GZMA + cells, Tn-CCR7 + cells, HSP-T-HSP + cells, Treg-Ctla4 + cells, and Trm-CD69 + cells. (**C**) t-SNE plot dividing T cells into two groups based on histidine metabolism levels: high histidine metabolism group(left) and low histidine metabolism group(right). (**D**) Proportions of T cell subpopulations within the high and low histidine metabolism level groups. (**E**) Heatmap showing intercellular communication intensities mediated by various signaling axes among different T-cell subpopulations. (**F**) Heatmap illustrating CLEC, MIF, SPP1, PARs, MHC-II, and VTN signaling intensities in the high and low histidine metabolism groups. (**G**) Bubble chart of GSEA outcomes for T-cell subpopulations in high vs. low histidine metabolism conditions. (**H**) Bubble chart of GO enrichment analysis showing how histidine metabolism affects T-cell function. (**I**) Representative flow cytometry gating strategies for mouse splenic lymphocytes and their differentiation, activation, and exhaustion status under different histidine concentrations. (**K**) The bar chart displays the differentiation, activation, and exhaustion of CD4 + T cells (upper) and CD8 + T cells (lower) after co-culture with different concentrations of histidine treatment. Error bars represent the SD from five independent experiments, $^{*}P < 0.05$, $^{**}P < 0.01$, $^{***}P < 0.001$

Overall, These findings further validated the conclusions from single-cell sequencing data analysis, as well as both in vivo and in vitro experiments, indicating that elevated histidine metabolism promotes tumor progression by modulating the tumor microenvironment, inhibiting immune cell infiltration and function.

Construction of a prognostic model for hepatocellular carcinoma based on elevated histidine metabolism

To construct a prognostic model for HCC related to histidine metabolism, we first analyzed the relationship between histidine metabolism-related genes and the clinical survival of HCC patients using the TCGA database. Eight genes were found to be significantly correlated with patient survival, with four identified as risk factors (Fig. 5A, B, Supplementary Fig. 9A). Next, we constructed a lasso prognostic model that incorporated seven genes (Fig. 5C). By combining the lasso prognostic model with survival correlation analysis, we identified two genes, AOC1 and BUD23, which influence HCC prognosis through histidine metabolism (Fig. 5D). We further analyzed the relationship between these two genes and clinical HCC features and found that BUD23 expression was correlated with tumor status, pathological T stage, pathological stage, and histological grade (Fig. 5E), and was negatively correlated with the infiltration of various immune cells (Fig. 5F, Supplementary Fig. 9C). By contrast, AOC1 expression showed no significant effect on tumor status or stage (Supplementary Fig. 9B), though it was positively correlated with infiltration by immunosuppressive cell populations (Fig. 5G, Supplementary Fig. 9C).

We constructed siRNAs targeting AOC1 or BUD23 to silence these genes in tumor cells (Supplementary Fig. 9D, E), and assessed the impact of these two genes on the metabolism of hepatocellular carcinoma cells using Seahorse experiments. After AOC1 interference, ATP-linked respiration decreased, non-mitochondrial oxygen consumption increased, while the glycolytic rate showed no significant change. After BUD23 interference, ATP-linked respiration also decreased, non-mitochondrial oxygen consumption decreased, and the glycolytic rate was significantly reduced (Fig. 5H, I, Supplementary Fig. 9F, G).

We further co-cultured the cells with THP-1–derived M0 macrophages and human peripheral blood lymphocytes after gene interference. Flow cytometry was used to evaluate T-cell function and macrophage polarization. In lymphocytes, BUD23 silencing increased the proportion of $CD4^+$ and $CD8^+$ T cells (Fig. 5J). The fraction of activated $CD69^+$ T cells and the mean fluorescence intensity of CD69 in both $CD4^+$ and $CD8^+$ T-cell populations rose, reflecting heightened T-cell activation. $PD1^+$ T-cell frequency decreased, with lower mean fluorescence intensity for PD1, indicating reduced T-cell exhaustion (Fig. 5K). Macrophages shifted more toward the M1 phenotype, while the proportion of tumor-promoting $CD163^+$ M2 macrophages declined, resulting in a reduced M2/M1 ratio. Conversely, silencing AOC1 had no discernible impact on T-cell function or macrophage polarization (Fig. 5L). These findings suggest that histidine metabolism primarily exerts its immunomodulatory effects through changes in glycolytic rate mediated by BUD23, making it a potential biomarker for predicting immunotherapy outcomes and a promising therapeutic target.

Additionally, we compared patients with high vs. low histidine metabolism in TCGA to identify differentially expressed genes, which were then used to build a prognostic model via multivariate Cox regression (Table 1). The findings revealed that patients classified in the high-risk group had notably shorter survival times and higher mortality rates (Supplementary Fig. 9H). Survival curves further confirmed that the high-risk group exhibited significantly worse outcomes than the low-risk group (Supplementary Fig. 9I). Performance evaluation of the model showed AUC values of 0.83 (overall prediction), 0.838 (3-year), and 0.841 (5-year) (Supplementary Fig. 9J, K), indicating strong predictive power for patient survival risk. Overall, patients in the high-risk group had a poorer prognosis, suggesting that gene alterations associated with histidine metabolism could be a critical factor influencing survival.

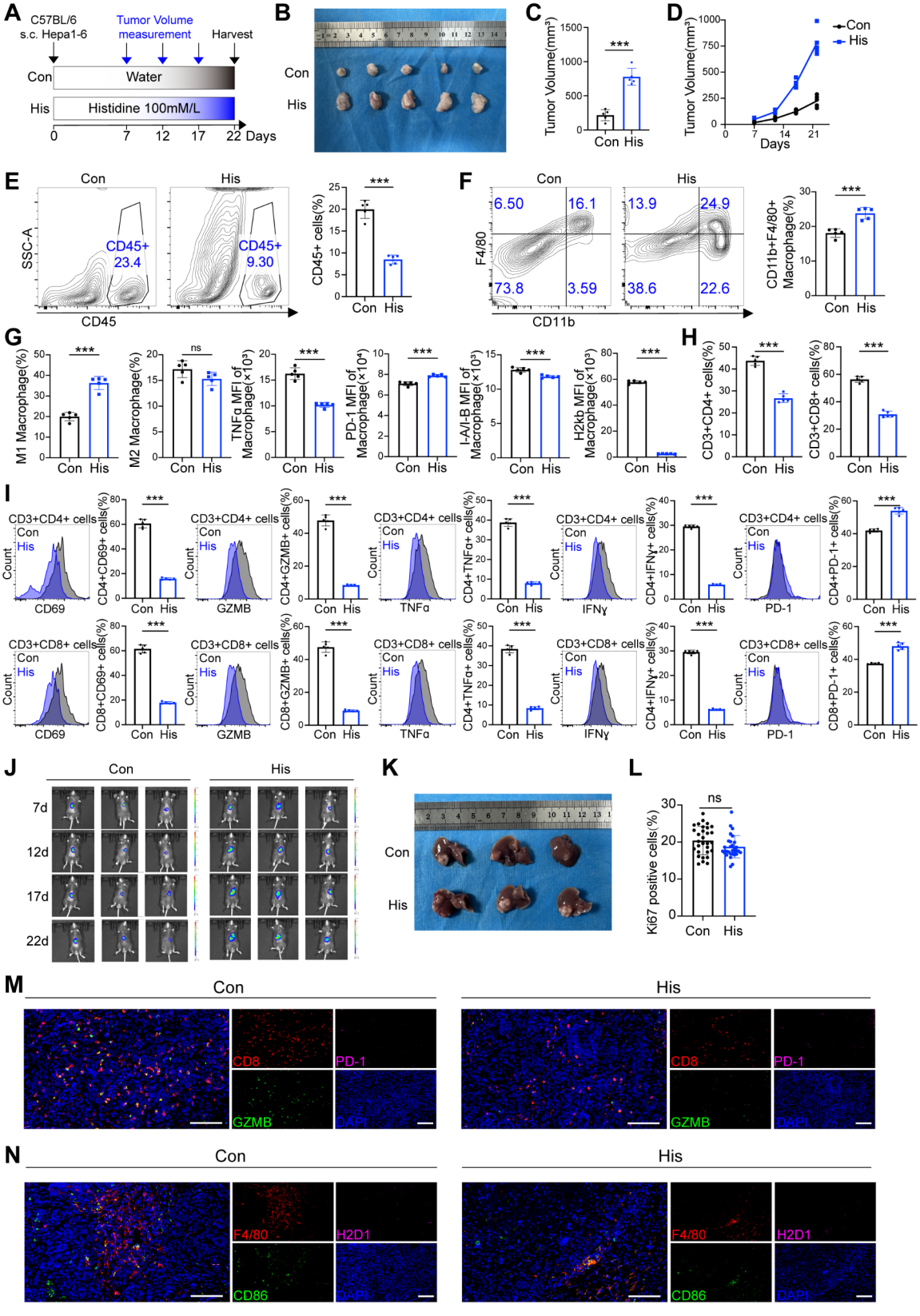

Fig. 4 (See legend on next page.)

(See figure on previous page.)

Fig. 4 High Histidine Metabolism Promotes Tumor Growth in Mice by Regulating the Tumor Microenvironment. (**A**) Schematic of the mouse subcutaneous HCC model. (**B**) Measurement of subcutaneous tumor size in the control and histidine-treated groups. (**C**) Quantitative analysis of tumor sizes from(**B**). (**D**) Tumor growth curves in mice from the control and histidine treatment groups. (**E–I**) Flow cytometric analysis of immune cell infiltration in subcutaneous tumors: (**E**) $CD45^+$ cells, (**F**) $CD11b^+F4/80^+$ macrophages, (**G**) polarization of macrophages into M1 and M2, and expression levels of TNFα, IFNγ, I-A/I-B, and H2Kb, (**H**) differentiation of CD4 + T cells and CD8 + T cells, (**I**) expression levels of CD69, GZMB, TNFα, IFNγ, and PD-1 in T cells. Error bars represent the SD from five independent experiments, ns, not significant, $^*P < 0.05$, $^{***}P < 0.001$. (**J**) Imaging of orthotopic liver tumor in mice from the control and the histidine treatment group. (**K**) Measurement of orthotopic liver tumor sizes in mice from the control and the histidine treatment group. (**L**) Representative Ki67 immunohistochemistry quantification. Ten fields per sample ($n = 30$). Error bars show mean ± SD, ns, not significant. (**M**, **N**) Representative immunofluorescence images and quantification. Scale bar = 100 μm

In summary, through single-cell sequencing data, TCGA data mining, along with both in vivo and in vitro experiments, we demonstrate that histidine metabolism reprograms tumor cell metabolism in HCC and reshapes the immune microenvironment—suppressing immune cell infiltration and modulating immune cell function—to drive tumor progression and impact patient prognosis. The expression of the histidine metabolism-related gene BUD23 is correlated with clinical stage, prognosis, and immune cell infiltration, and immune function, suggesting that BUD23 may serve as both a clinical biomarker for immunotherapy efficacy and a potential therapeutic target.

Discussion

This study, integrating single-cell sequencing data with in vivo and in vitro experiments, systematically unveils the pivotal regulatory role of histidine metabolism in the immune microenvironment of hepatocellular carcinoma (HCC). Our results indicate that high histidine metabolism not only reprograms metabolic pathways within tumor cells and stromal cells but also inhibits immune cell infiltration and function by affecting the communication between tumor cells, stromal cells, and immune cells, thereby promoting tumor progression. Furthermore, the histidine metabolism–related gene BUD23 has been identified as a potential prognostic marker and therapeutic target, broadening the mechanistic understanding of histidine metabolism in tumor biology.

Previous research has primarily focused on metabolic pathways involving glutamine and glucose and their effects on tumor immune evasion, while the role of histidine metabolism in HCC remains less explored [39]. By linking histidine metabolism to the HCC immune microenvironment, this study reveals a novel mechanism wherein metabolic reprogramming modulates immune cell function via intercellular communication networks. Specifically, high histidine metabolism, through tumor cell metabolic reprogramming and the downregulation of multiple intercellular signaling axes (e.g., MIF, CLEC, MHCII, SPP1), suppresses the antitumor activities of macrophages and T cells, thereby facilitating an immunosuppressive tumor microenvironment. This finding deepens our understanding of the interplay between metabolism and tumor immunity and supports the concept that metabolic reprogramming is a critical component of immune evasion.

Previous studies have shown that the histidine metabolite histamine regulates immune responses in the tumor microenvironment through different receptors [10, 14]. Consistent with these findings, our study confirms the inhibitory effect of histidine metabolism on immune cell function. Additionally, prior research has indicated that alterations in the expression of certain histidine metabolism-related products or enzymes in tumors may regulate metabolic reprogramming, thereby influencing tumorigenesis and progression [16, 40, 41]. However, unlike studies focusing solely on tumor cell proliferation or apoptosis, our study shows that histidine metabolism does not significantly alter intrinsic tumor proliferation, instead, it promotes tumor progression largely by immune suppression and microenvironmental remodeling. This discrepancy underlines that metabolic processes are not merely enhancing tumor cell proliferation but can also exert broader effects on immune cell function and immune–stromal interactions [42]. Monitoring and intervening in the dynamic interplay between tumor metabolism and immune function may hold greater therapeutic potential than merely inhibiting tumor proliferation.

The results of this study have significant clinical implications. First, the global regulation of the tumor immune microenvironment by histidine metabolism and its products presents potential targets for developing novel immunotherapy strategies. Specifically, intervening in histidine metabolic pathways may effectively enhance immune cell infiltration into tumors and improve their antitumor functions, thereby enhancing the efficacy of immunotherapy. Additionally, as histidine is an essential amino acid for the human body, interventions targeting its metabolic pathways through dietary intake could regulate metabolic reprogramming [43], providing an adjunctive strategy for liver cancer immunotherapy. The identification of the BUD23 gene provides new evidence for a molecular biomarker of prognosis in liver cancer patients. It can be used to guide personalized treatment strategies and

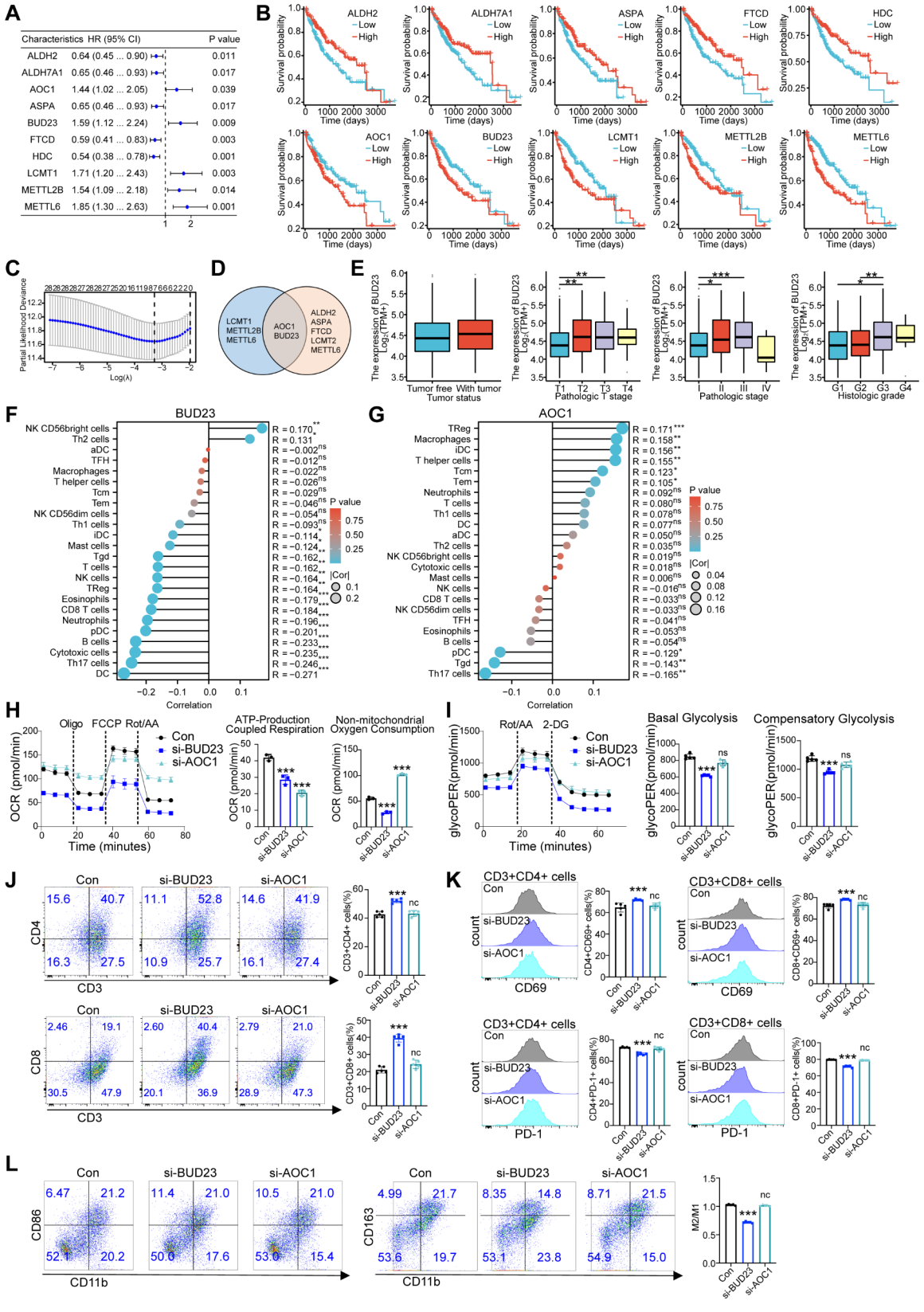

Fig. 5 (See legend on next page.)

(See figure on previous page.)

Fig. 5 Construction of a Prognostic Model for Hepatocellular Carcinoma Based on High Histidine Metabolism. (**A**) Forest plot displaying the association between histidine metabolism-related genes and the survival of liver cancer patients. (**B**) Kaplan-Meier survival curves for patients with histidine metabolism-related gene expression, analyzed using TCGA data. (**C**) Construction of a lasso prognostic model using histidine metabolism-related genes. (**D**) Venn diagram displaying genes included in both the lasso prognostic model and those associated with the survival of liver cancer patients. (**E**) TCGA data analysis of BUD23 gene expression and its association with tumor status, pathological T stage, pathological stage, and histological grade in liver cancer patients. (**F**) Correlation of BUD23 expression with infiltration of various immune cell types in TCGA data. (**G**) Correlation of AOC1 expression with infiltration of various immune cell types in TCGA data. (**H**) Seahorse analysis of the impact of BUD23 and AOC1 expression on oxygen consumption rate (OCR). (**I**) Seahorse analysis of the impact of BUD23 and AOC1 expression on glycolytic rate (glycoPER). (**K**) Flow cytometry assessing the effects of BUD23 or AOC1 knockdown on T-cells differentiation: $CD3^+CD4^+$ T cells (upper), $CD3^+CD8^+$ T cells (lower). (**L**) Flow cytometry assessing the effects of BUD23 or AOC1 knockdown on T-cells function: CD69 expression (upper), PD-1 expression (lower). (**L**) Flow cytometry examining macrophage polarization following BUD23 or AOC1 knockdown. Error bars represent the SD of three or five independent experiments, ns, not significant, $^{***}P < 0.001$

serve as a predictive indicator of the effectiveness of immunotherapy.

Despite using multiple approaches to confirm the role of histidine metabolism in hepatocellular carcinoma (HCC), this study has some limitations. First, single-cell sequencing data were predominantly sourced from public repositories (e.g., GEO, TCGA), meaning the sample sizes and patient populations—including racial backgrounds—were relatively restricted. Large-scale, multicenter cohorts would be needed to validate the generalizability of these findings and enhance their clinical translational value. Although mouse subcutaneous and orthotopic liver cancer models partially recapitulate aspects of the HCC microenvironment, they still differ from human liver anatomy and immune characteristics. Future work employing organoid systems or humanized mouse models may better approximate the actual pathophysiological conditions. Additionally, the lack of transgenic mouse models, such as BUD23 knockout mice, limits the ability to confirm the specific role of BUD23 in liver cancer progression in vivo. Using a transgenic model could provide a more specific and direct understanding of the mechanistic pathways regulated by BUD23 and its influence on tumor growth and immune regulation. Second, histidine metabolism does not operate in isolation. Rather, it intersects with other pathways, including amino acid, glycolytic, and fatty acid metabolism. While this study provides preliminary evidence linking histidine metabolism to tumor cell energy metabolism, the exact mechanisms by which these metabolic processes shift and collectively drive tumor growth remain incompletely understood. Furthermore, BUD23 has emerged as a key gene related to prognosis and immune microenvironment regulation in HCC, yet its specific signaling pathways await detailed exploration. For example, it remains uncertain whether BUD23 intersects common immune regulatory pathways such as mTOR, NF-κB, or MAPK, and whether it carries potential as a therapeutic target. Clinical confirmation of BUD23 expression and its correlation with immunotherapy responses will help determine its clinical utility as a molecular biomarker. Finally, although this study reveals the impact of histidine metabolism on immune cell functionality, the precise regulatory mechanisms underlying tumor progression require additional investigation, especially regarding the feasibility of pharmacologically targeting these mechanisms.

This study provides a new perspective on the critical role of histidine metabolism in shaping the immune microenvironment of hepatocellular carcinoma (HCC) and reveals the mechanism by which it promotes tumor progression through metabolic reprogramming, impacting the functions of macrophages and T cells. These findings offer new potential targets for future liver cancer treatment strategies, particularly in the context of immunotherapy, and lay a theoretical foundation for personalized treatment and prognosis evaluation of liver cancer patients. Future research should further explore additional functions of histidine metabolism and its role in other cancer types, with the aim of achieving broader clinical applications.

Table 1 Multivariate cox regre

id	coef	HR	HR.95L	HR.95H	pvalue
PKIB	-0.84195	0.430871	0.25416	0.730445	0.00177
ADH4	-0.38965	0.677291	0.420615	1.090601	0.108904
ENO2	-2.19664	0.111176	0.046879	0.263658	6.17E-07
GAGE4	-0.45822	0.632407	0.427316	0.935931	0.021962
TRNP1	0.747976	2.112719	1.068206	4.178577	0.031588
NKX3-2	0.197226	1.218019	0.960558	1.544488	0.103561
GAGE2D	0.820159	2.270861	1.554614	3.3171	2.21E-05
KCTD17	1.071959	2.921095	1.250961	6.820995	0.013232
G6PC	0.897332	2.453049	0.879041	6.845472	0.086576
FTCD	-1.19708	0.302075	0.177086	0.515283	1.12E-05
EPO	0.783374	2.188845	1.699767	2.818647	1.27E-09
MMP7	0.312523	1.366869	1.070147	1.745864	0.012317
SMOX	1.234923	3.438114	1.173919	10.06937	0.024295
MMP1	0.367296	1.443825	1.085175	1.921011	0.011702
LECT2	-0.45474	0.63461	0.424261	0.949251	0.026865
TDRD5	-0.26537	0.766922	0.609749	0.964608	0.023334
ALDH5A1	4.264317	71.11632	5.992486	843.9787	0.000729
LRP2	0.238742	1.269651	1.048714	1.537134	0.014381
NR0B1	0.25117	1.285529	1.054138	1.56771	0.013113
FBXO41	0.77419	2.168834	1.195532	3.934518	0.010845
OGDHL	-0.78104	0.457931	0.290476	0.721922	0.000771
SPP1	1.117485	3.057155	1.610613	5.802884	0.000632
SGPP2	-0.22623	0.797535	0.616352	1.03198	0.085332
MMP10	-0.2099	0.810665	0.630859	1.04172	0.100898
HULC	-0.66471	0.514421	0.272077	0.972623	0.040817
EGLN3	0.508033	1.662018	0.971234	2.844117	0.063814
TCP10L	-0.32064	0.725686	0.496171	1.061369	0.098345
TMPRSS6	-1.12052	0.326112	0.111807	0.951184	0.040209
SOX11	0.373482	1.452784	1.1308	1.86645	0.003483
TRIM55	-0.21634	0.805464	0.641619	1.011148	0.062263
HMGCS2	-2.23533	0.106957	0.028939	0.395306	0.000804
HPX	1.834683	6.263149	1.030005	38.08432	0.046364
PLIN5	-1.91668	0.147095	0.036844	0.587263	0.006657
RNF24	-1.84599	0.157869	0.046048	0.541224	0.003318
RBP4	2.922583	18.58925	1.830195	188.8105	0.013474
TMC5	-0.37322	0.688517	0.515445	0.919701	0.011515
CYP2C9	0.746216	2.109004	0.986021	4.510959	0.054396
F11	0.860832	2.365127	0.948068	5.900241	0.064947
CYP17A1	-0.31915	0.726765	0.559371	0.944252	0.016875
PCLO	0.239566	1.270698	1.015112	1.590636	0.03654
RAMP1	-0.52326	0.592586	0.297851	1.178975	0.135998
SLC10A1	0.663109	1.940816	1.18829	3.169906	0.008069
ZPLD1	-0.27031	0.763143	0.619867	0.939535	0.010839

Abbreviations

HCC	Hepatocellular carcinoma
TCGA	The Cancer Genome Atlas
BUD23	Putative N7-guanosine methyltransferase
MIF	Macrophage Migration Inhibitory Factor
MHC II	Class II Major Histocompatibility Complex
t-SNE	t-Distributed Stochastic Neighbor Embedding
GEO	Gene Expression Omnibus
siRNA	Small interfering RNAs
PMA	Phorbol 12-myristate 13-acetate
GSEA	Gene Set Enrichment Analysis
KEGG	Kyoto Encyclopedia of Genes and Genomes
GO-BP	Gene Ontology-Biological Process
GSVA	Gene Set Variation Analysis
AOC1	Amine oxidase copper-containing 1
FBS	Fetal bovine serum
IHC	Immunohistochemistry
H&E	Hematoxylin and Eosin
HSP	Heat shock proteins
IFN	Interferon
TNF	Tumor Necrosis Factor
GZM	Granzyme

Supplementary Information

The online version contains supplementary material available at https://doi.org/10.1186/s12967-025-06267-y .

Supplementary Material 1

Acknowledgements
Not applicable.

Author contributions
Pengcheng Liu was involved in protocol design, in vitro and in vivo experiments, data analysis, and drafting the manuscript; Fuxin Huang was involved in protocol design and single-cell sequence analysis. Peixu Lin was involved in in vitro and in vivo experiments. Pincheng Zhou was involved in in vitro experiments and data analysis. Jie Wang was involved in in vivo experiments and data analysis. Huanhuan Sun, Fan Xing and Haiqing Ma were involved in grant support, protocol design, and manuscript review. All authors read and approved the final manuscript.

Funding
The work was supported by The National Natural Science Foundation of China (82072719), the Natural Science Foundation of the Guangdong Province (2021A1515010790, 2023A1515012872) and High-level Hospital Construction Research Project of Heyuan People's Hospital (YNKT202203).

Data availability
Upon reasonable request, the data supporting the conclusions of this paper will be made available by the corresponding author.

Declarations

Ethics approval and consent to participate
The study was approved by the Ethical Review Committee of the Guangdong Provincial People's Hospital and was conducted in accordance with the Declaration of Helsinki (Project No. S2024-816-01).

Consent for publication
All authors agreed on the manuscript.

Conflict of interest
The authors declare no potential conflicts of interest.

Author details
[1]Medical Research Institute, Guangdong Provincial People's Hospital (Guangdong Academy of Medical Sciences), Southern Medical University School of Medicine, Guangzhou 510006, China
[2]Department of Oncology, Heyuan Hospital of Guangdong Provincial People's Hospital, Heyuan People's Hospital, Heyuan 517000, China
[3]School of Medicine, South China University of Technology, Guangzhou 510006, China
[4]Guangdong Cardiovascular Institute, Guangdong Provincial People's Hospital, Guangdong Academy of Medical Sciences, Guangzhou 510006, China

Received: 15 December 2024 / Accepted: 14 February 2025
Published online: 04 March 2025

References

1. Agus A, Clement K, Sokol H. Gut microbiota-derived metabolites as central regulators in metabolic disorders. Gut. 2021;70(6):1174–82.
2. Holeek M. Histidine in Health and Disease: Metabolism, Physiological Importance, and Use as a Supplement[J]. Nutrients. 2020;12(3):848. https://doi.org/10.3390/nu12030848
3. Johansson PI, et al. LASSO regression shows histidine and sphingosine 1 phosphate are linked to both sepsis mortality and endothelial damage. Eur J Med Res. 2024;29(1):71.
4. Llovet JM, et al. Hepatocellular carcinoma. Nat Rev Dis Primers. 2021;7(1):6.
5. Mak LY, Liu K, Chirapongsathorn S, et al. Liver diseases and hepatocellular carcinoma in the Asia-Pacific region: burden, trends, challenges and future directions[J]. Volume 21. Nature Reviews Gastroenterology & Hepatology; 2024. pp. 834–51. 12.
6. Yang X, et al. Precision treatment in advanced hepatocellular carcinoma. Cancer Cell. 2024;42(2):180–97.
7. Brosnan ME, Brosnan JT. Histidine metabolism and function. J Nutr. 2020;150(Suppl 1):S2570–5.
8. Ghassem Zadeh R, Yaylayan V. Interaction pattern of histidine, carnosine and Histamine with Methylglyoxal and other carbonyl compounds. Food Chem. 2021;358:129884.
9. O'Mahony L, Akdis M, Akdis CA. Regulation of the immune response and inflammation by Histamine and Histamine receptors. J Allergy Clin Immunol. 2011;128(6):1153–62.
10. Tiligada E, et al. Opportunities and challenges in the therapeutic exploitation of Histamine and Histamine receptor Pharmacology in inflammation-driven disorders. Pharmacol Ther. 2024;263:108722.
11. Smolinska S, et al. Histamine and gut mucosal immune regulation. Allergy. 2014;69(3):273–81.
12. Li H, et al. The allergy mediator Histamine confers resistance to immunotherapy in cancer patients via activation of the macrophage Histamine receptor H1. Cancer Cell. 2022;40(1):36–e529.
13. Chen J, et al. Glioblastoma stem cell-specific Histamine secretion drives pro-angiogenic tumor microenvironment remodeling. Cell Stem Cell. 2022;29(11):1531–e15467.
14. Chen S, Luster AD. Antihistamines for cancer immunotherapy: more than just treating allergies. Cancer Cell. 2022;40(1):9–11.
15. Horn P, Tacke F. Metabolic reprogramming in liver fibrosis. Cell Metab. 2024;36(7):1439–55.
16. Lin J, et al. Metabolic reprogramming in the tumor microenvironment of liver cancer. J Hematol Oncol. 2024;17(1):6.
17. Yang F, et al. Metabolic reprogramming and its clinical implication for liver cancer. Hepatology. 2023;78(5):1602–24.
18. Feng J, et al. Emerging roles and the regulation of aerobic Glycolysis in hepatocellular carcinoma. J Exp Clin Cancer Res. 2020;39(1):126.
19. Loomba R, Friedman SL, Shulman GI. Mechanisms and disease consequences of nonalcoholic fatty liver disease. Cell. 2021;184(10):2537–64.
20. Paul B, Lewinska M, Andersen JB. Lipid alterations in chronic liver disease and liver cancer. JHEP Rep. 2022;4(6):100479.
21. Du D, et al. Metabolic dysregulation and emerging therapeutical targets for hepatocellular carcinoma. Acta Pharm Sin B. 2022;12(2):558–80.
22. Bernard JJ, Gallo RL, Krutmann J. Photoimmunology: how ultraviolet radiation affects the immune system. Nat Rev Immunol. 2019;19(11):688–701.
23. Koh A, et al. From dietary Fiber to host physiology: Short-Chain fatty acids as key bacterial metabolites. Cell. 2016;165(6):1332–45.

24. Sun X, et al. Histidine supplementation alleviates inflammation in the adipose tissue of high-fat diet-induced obese rats via the NF-kappaB- and PPARgamma-involved pathways. Br J Nutr. 2014;112(4):477–85.
25. Yan-Chuan L, Chun-Long L, Jia-Yue Q, et al. Relationships of dietary histidine and obesity in Northern Chinese adults, an Internet-Based Cross-Sectional Study[J]. Nutrients. 2016;8(7):420.
26. Watanabe M, et al. Consequences of low plasma histidine in chronic kidney disease patients: associations with inflammation, oxidative stress, and mortality. Am J Clin Nutr. 2008;87(6):1860–6.
27. Niu YC, et al. Histidine and arginine are associated with inflammation and oxidative stress in obese women. Br J Nutr. 2012;108(1):57–61.
28. Feng RN, et al. Histidine supplementation improves insulin resistance through suppressed inflammation in obese women with the metabolic syndrome: a randomised controlled trial. Diabetologia. 2013;56(5):985–94.
29. Rebouissou S, Nault JC. Advances in molecular classification and precision oncology in hepatocellular carcinoma. J Hepatol. 2020;72(2):215–29.
30. Leone V, et al. Liver inflammation and hepatobiliary cancers. Trends Cancer. 2021;7(7):606–23.
31. Brahma MK, et al. Oxidative stress in obesity-associated hepatocellular carcinoma: sources, signaling and therapeutic challenges. Oncogene. 2021;40(33):5155–67.
32. Huang Z, et al. Oxidative stress promotes liver Cancer metastasis via RNF25-Mediated E-Cadherin protein degradation. Adv Sci (Weinh). 2024;11(13):e2306929.
33. Froldi F, Pachnis P., Milán Szuperák,et al.histidine is selectively required for the growth of Myc-dependent dedifferentiation tumours in the Drosophila CNS[J]. EMBO J. 2019;38(7):e99895.
34. Kennedy L, et al. Blocking H1/H2 Histamine receptors inhibits damage/fibrosis in Mdr2(-/-) mice and human cholangiocarcinoma tumorigenesis. Hepatology. 2018;68(3):1042–56.
35. Chen X, et al. Histidine decarboxylase (HDC)-expressing granulocytic myeloid cells induce and recruit Foxp3(+) regulatory T cells in murine colon cancer. Oncoimmunology. 2017;6(3):e1290034.
36. Jiao Y, et al. Acetylcholine promotes chronic stress-induced lung adenocarcinoma progression via alpha5-nAChR/FHIT pathway. Cell Mol Life Sci. 2023;80(5):119.
37. Xia L, et al. The cancer metabolic reprogramming and immune response. Mol Cancer. 2021;20(1):28.
38. Martinez-Reyes I, Chandel NS. Cancer metabolism: looking forward. Nat Rev Cancer. 2021;21(10):669–80.
39. Pavlova NN, Thompson CB. Emerg Hallm Cancer Metabolism Cell Metab. 2016;23(1):27–47.
40. Wang Y, et al. PKM2 functions as a histidine kinase to phosphorylate PGAM1 and increase Glycolysis shunts in cancer. EMBO J. 2024;43(12):2368–96.
41. Mossmann D, et al. Arginine reprograms metabolism in liver cancer via RBM39. Cell. 2023;186(23):5068–e508323.
42. Pavlova NN, Zhu J, Thompson CB. The hallmarks of cancer metabolism: still emerging. Cell Metab. 2022;34(3):355–77.
43. Warmbrunn MV, et al. Oral histidine affects gut microbiota and MAIT cells improving glycemic control in type 2 diabetes patients. Gut Microbes. 2024;16(1):2370616.

Publisher's note